J Mater Sci (2011) 46:1613–1621
DOI 10.1007/s10853-010-4975-5

# Sb-doped $CuAlO_2$: widening of band gap and nonlinear *J–E* characteristics

**C. K. Ghosh · S. R. Popuri · D. Sarkar · K. K. Chattopadhyay**

Received: 21 May 2010 / Accepted: 4 October 2010 / Published online: 23 November 2010

**Abstract** The effect of antimony doping on the optical and electrical properties of copper aluminum oxide synthesized by solid state reaction technique was investigated. Formation of single phase $CuAlO_2$ was confirmed by x-ray diffraction studies. Variation of strain, particle size, and preferred orientation of the crystallites with Sb doping concentrations were analyzed by x-ray diffraction. Using the x-ray photoelectron spectroscopy trivalent state of Sb ions was confirmed. A blue shift in the energy band gap with Sb doping was observed, and it was supported by ab initio calculation based on density functional theory. A nonlinear current–voltage characteristic was observed for the Sb-doped $CuAlO_2$ samples whereas the same was linear for the undoped samples. The nonlinearity of the current–voltage characteristics changed significantly at higher temperature, and this behavior was explained.

## Introduction

The transparent conducting oxides (TCOs) are a class of semiconducting materials which are transparent in the visible region of the electromagnetic spectrum with a high electrical conductivity. Wide spread interests in TCOs are due to their interesting electrical and optoelectronic properties, which qualify them as a promising candidate for various technological applications such as transparent electrodes in flat panel display [1], window layers in solar cell [2], liquid crystal display [3], organic light-emitting diode [4], transparent thin film transistor [5], UV-emitting diode [6], photovoltaic cell [7], catalysis [8], thermoelectrics [9] etc. It is well known that most of the common TCOs like tin oxide ($SnO_2$) [10], indium tin oxide (ITO) [11], cadmium oxide (CdO) [12], zinc oxide (ZnO) [13] etc. are all n-type semiconductors (electrons are majority carriers). Along with various applications utilizing the linear current density–electric field (*J–E*) characteristics in the above mentioned fields, nonlinear *J–E* characteristics observed in different doped TCOs such as Sb-doped $SnO_2$ [14], F-doped $SnO_2$ [15], F-doped CdO [16], made them also potential candidates in the field of power supply network and electrical stress grading at insulator–conductor interface in high voltage applications [17]. There are also a few reports on the p-type conducting oxides such as CuO [18], but they are not transparent in the visible region of the electromagnetic spectrum. The primary advantage of $CuAlO_2$ (CAO) is that, it exhibits p-type semiconducting behavior and shows transparency in the visible region. However, the electrical conductivity of CAO was 2–3 orders of magnitude lower than that of the most commonly used n-type TCOs like ITO. Therefore, the improvement of the electrical conductivity of CAO seems very exigent and necessary for practical applications. Effect of doping by divalent ionic species on the electrical properties of CAO was investigated by many researchers [19, 20]. We have also examined the effect of excess oxygen on the electrical property of CAO [21]. Field emission property and thermoelectric effects of CAO were reported by our research group [22, 23]. We have also fabricated all oxide transparent heterojunction (n-ZnO/p-$CuAlO_2$) that proves itself a potential candidate for the invisible electronics [24]. There are a few reports on the magnetic properties of

---

C. K. Ghosh · K. K. Chattopadhyay (✉)
School of Materials Science and Nanotechnology,
Jadavpur University, Kolkata 700032, India
e-mail: kalyan_chattopadhyay@yahoo.com

S. R. Popuri · D. Sarkar · K. K. Chattopadhyay
Thin Film and Nano-Science Laboratory, Department of Physics,
Jadavpur University, Kolkata 700032, India

transitional metal-doped CAO [25, 26]. However, there is no report on the effect of doping by trivalent non-transitional metal elements such as Sb on the optical and electrical properties of CAO whereas effect of Sb doping on the other delafossite materials had been studied previously [27, 28]. The aim of this article is to study the effect of Sb doping on the structural, optical, and electrical properties of CAO. To support our experimental observations, we have also performed ab initio calculations based on the density functional theory.

## Experimental details

### Sample preparation

$CuAl_{1-x}Sb_xO_2$ ($x = 0.02$, 0.04, 0.06, and 0.08) powders were synthesized by solid state reaction method. Stoichiometric mixtures of high purity $Cu_2O$ (Aldrich 99.99%), $Al_2O_3$ (Aldrich 99.99%), and $Sb_2O_3$ (Alfa Aesar, 99.6%) powders were mixed for 2 h. Then the mixtures were sintered in a furnace in open air at 1150 °C for 12 h to obtain the Sb-doped CAO samples. Finally, the sintered powders were grounded and pressed into pellets by a hydrostatic pressure of 100 Kgf/cm$^2$. The obtained pellets were again sintered at 1100 °C and were used for further characterizations.

### Characterization

The synthesized powders were characterized by x-ray diffraction technique (XRD, BRUKER D8 ADVANCE, by Cu Kα radiation, $\lambda = 1.5404$ Å). X-ray photoelectron spectroscopic (Specs, Germany) measurement was carried out using a dual anode source and a hemispherical analyzer (HSA 3500) operating in a constant pass energy mode. Measurement was carried out by using Al *Kα* radiation (1486.6 eV) and with pass energy of 40 eV. The base pressure of the sample analysis chamber was $2.8 \times 10^{-9}$ mbar. Analyses of the oxidation states from the spectra were performed by deconvolution using the Shirley background correction with the CASA software. Optical absorption spectra of the prepared Sb-doped CAO samples were measured by a UV–vis-NIR spectrophotometer (SHIMADZU-UV-3101-PC) in the wavelength range from 200 to 800 nm. $CuAlO_2$ powders were dispersed in alcohol and were sonicated for 5 min. Then on clean glass slide substrates $CuAlO_2$, thin films were deposited by dip coating method for optical measurement. The electrical characterizations of the SCAO samples were carried out by home made two probe electrical set up from room temperature (300 K) to 415 K under vacuum condition ($10^{-5}$ mbar). Electrical contacts were made with conducting silver paste (Arora Mathey) which was found to be Ohmic (showing linear *I*–*V* characteristics) within the entire range of applied voltage. Ohmic nature of the silver paste contacts have been confirmed previously by different researchers also [29–32].

## Results and discussion

### Structural property

X-ray diffraction pattern of the Sb-doped CAO samples ($CuAl_{1-x}Sb_xO_2$, $x = 0.02$, 0.04, 0.06, and 0.08, SCAO) are shown in Fig. 1. The XRD pattern clearly matches with the polycrystalline delafossite structure of CAO (space group: *R*3*m,* PDF 35–1401) and rules out the possibility of any secondary phase formation.

The increment in the full width at half maximum (FWHM, $\beta$) of the peaks with Sb doping indicates the reduction of grain size and also increment of the strain with Sb doping. Variation of grain size ($D$) and strain ($\varepsilon$) of CAO powder with Sb doping was calculated from the well known Williamson–Hall relation [33]

$$\beta\cos\theta/\lambda = 1/D + \varepsilon\sin\theta/\lambda \qquad (1)$$

and are shown in Fig. 2. The increase in strain is due to the larger ionic radius of $Sb^{+3}$ (0.76 Å) [34] compared to $Al^{+3}$ (0.675 Å) [35]. Equilibrium particle size ($r_0$) is mainly determined by surface energy ($\sigma_s$) and volume energy ($\sigma_v$) that includes strain and it is given by $r_0 = 2\sigma_s/\sigma_v$ [36]. The main contribution to surface energy originates from dangling bonds (depends on the shape of the particle) and energy associated with dangling bond that depends on oxidation state of the atoms, more precisely on the electronegativity differences between the anion and the

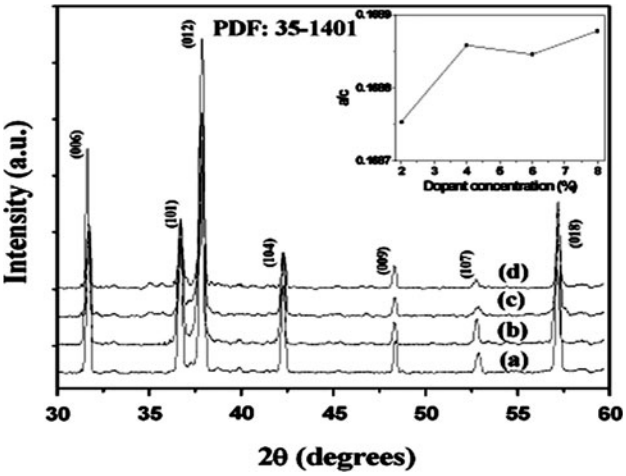

**Fig. 1** X-ray diffraction patterns of *a* 2%, *b* 4%, *c* 6%, and *d* 8% Sb-doped CAO (*inset* shows variation of *a*/*c* ratio with Sb doping)

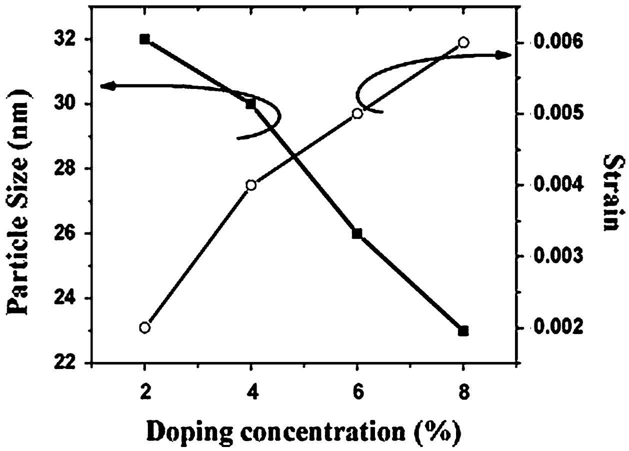

**Fig. 2** Variation of particle size and strain with Sb doping concentration

cation [37]. Since the particle shape is not changing, so the dangling bond remains same. If Sb be present at the Al site within the lattice as well as at the grain boundary region, its binding energy corresponding to two different types of Sb present in the system (within lattice and at the grain boundary) will be different but we have observed no asymmetry in XPS Sb 3*d* peak (discussed in Sect. Chemical state analysis and valence band structure determination by photoelectron spectroscopy; ab initio density of states calculation), so we may conclude that major portion of Sb is present within the lattice site. Even if small fraction of Sb were present at the grain boundaries, they will reduce the surface strain energy further because the electronegativity difference between Sb (1.88 [38]) and O (3.44 [39]) is less than the electronegativity differences between Al (1.5 [40]) and O. So we may neglect that the change in surface energy due to presence of very small fraction of Sb at grain boundary. However, strain contribution to volume energy will increase with Sb doping due to larger ionic radius of $Sb^{+3}$ than that of $Al^{+3}$. Therefore, we may predict that grain size will decrease due to enhancement of strain contribution to total volume energy. Lattice constants (*a*, *c*) were calculated from the relation between inter planar spacing and lattice constants of hexagonal crystal structure described elsewhere [41]. An enhancement in *a*/*c* ratio (shown in the inset of Fig. 1) with respect to Sb doping suggests that lattice parameter '*a*' is increasing due to substitution of $Al^{+3}$ by $Sb^{+3}$. The preferential orientation of the crystallites along (hkl) crystal plane in the samples were analyzed by calculating the texture coefficient $C_i$ of each XRD peak according to the relation [42]

$$C_i = \frac{N(I_i/I_{i0})}{\sum_{i=1}^{N}(I_i/I_{i0})} \qquad (2)$$

where $C_i$ is the texture coefficient of the *i*th plane, $I_i$ is the measured integral intensity, $I_{i0}$ is the integral intensity of the JCPDS-PDF of the corresponding peak *i*, and *N* is the number of the reflections considered for the analysis. $C_i$ is unity for each reflection in case of a randomly oriented sample, and values of the $C_i$ greater than unity indicate preferential orientation of the crystallites in that particular direction. In this case (107), (018) planes for 2% and (104), (006), (107) planes for 4% Sb-doped $CuAlO_2$ samples showed preferential orientations. The degree of preferential orientation of the sample as a whole, $\Omega$, can be assessed by estimating the standard deviation of all the $C_i$ values calculated for the sample [33],

$$\Omega = \sqrt{\frac{\sum_{i=1}^{N}(C_i - C_{i0})^2}{N}} \qquad (3)$$

where $C_{i0}$ is the texture coefficient of the powder sample, which is always unity. The value of $\Omega$ gives the degree of the orientation of the sample as a whole and can be used to compare the degree of preferential orientation (may not be in a particular/specific direction) of different samples. A value of zero for $\Omega$ indicates complete randomness of the whole sample and on the other hand, higher value of $\Omega$ suggests better preferential orientation of the prepared samples as whole. The texture coefficients of all the observed peaks of SCAO samples, along with the value of $\Omega$ for each concentrations are shown in Table 1. Here, it is observed that the degree of preferential orientation of CAO sample as a whole continuously increases with Sb doping. Similar types of results were also obtained previously by different researchers [43–46].

## Chemical state analysis and valence band structure determination by photoelectron spectroscopy; ab initio density of states calculation

Chemical composition and valence states of the atoms present in SCAO were investigated by XPS. Sb concentrations as determined from the XPS analysis were 1.93, 3.92, 5.90, and 7.85% corresponding to nominal compositions of 2.00, 4.00, 6.00, and 8.00% in the samples,

**Table 1** The texture coefficient (*C*) and the degree of preferential orientation ($\sigma$) for Sb-doped CAO

| %Sb | Texture coefficient (*C*) | | | | | | | $\Omega$ |
|---|---|---|---|---|---|---|---|---|
| | (006) | (101) | (012) | (104) | (009) | (107) | (018) | |
| 2 | 0.8680 | 0.8104 | 0.8379 | 0.9432 | 0.9220 | 1.2140 | 1.4042 | 0.21 |
| 4 | 1.3639 | 0.6149 | 0.5997 | 1.1729 | 0.7262 | 1.8221 | 0.7001 | 0.43 |
| 6 | 0.1507 | 0.0764 | 0.1147 | 0.1314 | 0.2462 | 0.1841 | 0.1352 | 0.85 |
| 8 | 0.1202 | 0.1201 | 0.1194 | 0.1660 | 0.1315 | 0.1299 | 0.2126 | 0.86 |

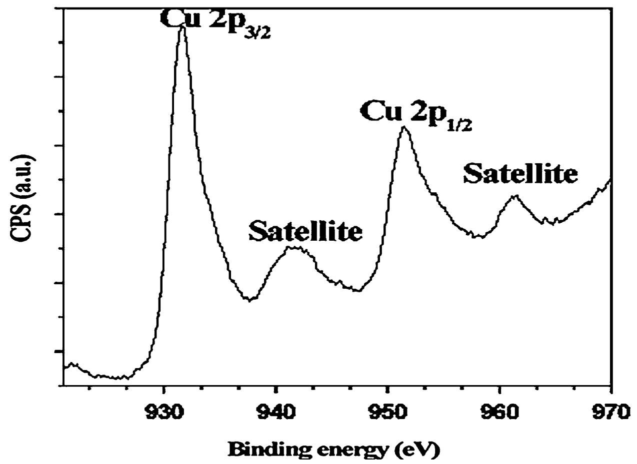

**Fig. 3** X-ray photoelectron spectra of Cu $2p_{3/2}$ and Cu $2p_{1/2}$ levels

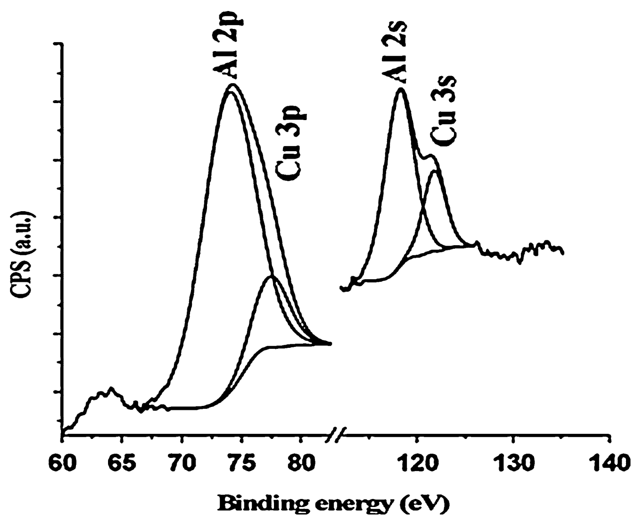

**Fig. 4** X-ray photoelectron spectra of Al $2p$, $2s$ and Cu $3p$, $3s$ levels

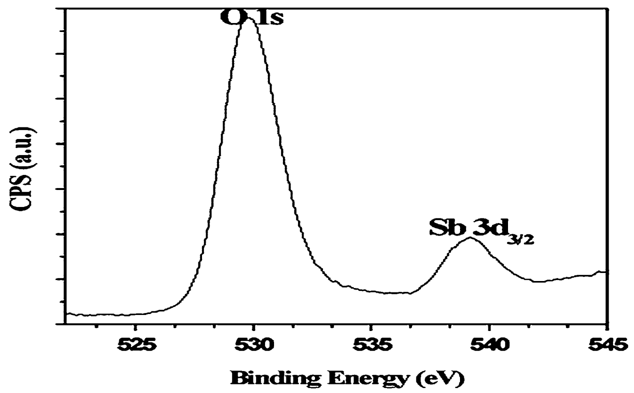

**Fig. 5** X-ray photoelectron spectra of Sb $3d_{3/2}$ and O $1s$ levels

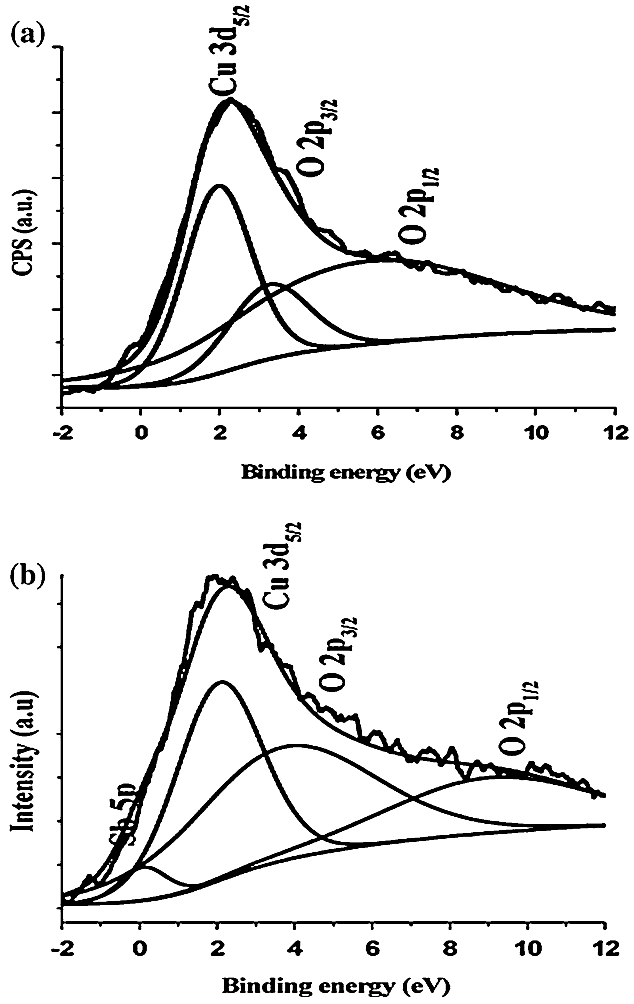

**Fig. 6** **a** Low lying energy levels of pure CAO. **b** Low lying energy levels of 6% Sb-doped CAO

respectively. The XPS spectra of SCAO covering Cu $2p$, Al $2p$ and Al $2s$ and Sb $3d$ and O $1s$ core level are shown in Figs. 3, 4, and 5 respectively. From Fig. 3 it is clear that, the binding energies of the Cu $2p_{3/2}$ and Cu $2p_{1/2}$ are found at 931.63 and 951.47 eV, respectively. The binding energies of the Al $2p$, Al $2s$, and O $1s$ levels are found at 73.7, 118.3 (Fig. 4), and 531.2 eV (Fig. 5). Detailed XPS analysis of copper, aluminum, and oxygen present in CAO has been described elsewhere [47]. There is no difference in binding energies of different core level energies corresponding to copper, aluminum, and oxygen in the case of CAO and SCAO. Low lying energy levels of pure CAO and 6% Sb-doped CAO samples are shown in Fig. 6a and b, respectively. From the figures it is clear that a valence band maximum in the case of SCAO samples shifts toward higher binding energy side compared to pure CAO. In pure CAO, valence band originates from Cu $3d$ and O $2p$ states as predicted by Kawazoe et al. [19] on the basis of chemical modulation of valence band. Binding energies of different low lying energy levels of copper $3d$ and oxygen $2p$ in pure CAO are listed in Table 2. After deconvoluting the low lying energy spectra of the Sb-doped CAO, we have obtained the binding energies of Cu $3d$ and O

**Table 2** Low lying binding energies (in eV) of different energy levels of copper (2*p*) and oxygen (2*p*) in pure CAO and Sb-doped CAO

| Sample | Cu (in eV) | O (in eV) | |
|---|---|---|---|
| | 3*d* | $2p_{1/2}$ | $2p_{3/2}$ |
| CAO | 1.98 | 3.36 | 6.15 |
| 6% Sb-doped CAO | 2.11 | 4.09 | 9.28 |

2*p* orbitals, and they are also listed in Table 2. Binding energy of Sb 5*p* orbital is measured at −0.15 eV. The electron–electron (Sb 5*p*–O 2*p* and Cu 3*d*) Coulomb repulsion may be responsible for the observed shift in valence band maximum.

To support our experimental observation, we have also performed ab initio band structure calculation of pure CAO and SCAO on the basis of density functional theory using super cells approach. The calculation was carried out by using CASTEP package provided by the Material Studio 4.1 developed by Accelrys. It is an ab initio quantum mechanical code based on density functional theory. Here, pseudo-potential is being considered for ionic potential, the electronic wave function is expanded on the basis of plane wave, and the exchange and correlative potential of electron–electron interactions are improved by the generalized gradient approximation (GGA). In this calculation, 1 × 1 × 1 Monkhorst–Pack k-point mesh was fixed within the Brillouin zone. Energy cutoff and precision were set at 500 eV and $2.0 \times 10^{-4}$ eV/atom, respectively. Here, 2 × 2 × 2 super cell was set because of our computational limitation, and it corresponds to 12.5% of Sb doping. Density of states (DOS) of pure CAO and 12.5% Sb-doped CAO are shown in Figs. 7 and 8, respectively. Three peaks are distinguishable in the valence band region approximately at −1.8, −3.4, and −6.1 eV (indexed I–III in Fig. 10a). Similar kind of results was also obtained by Aston et al. [48]. The Cu partial density of states (PDOS) is dominated by 3*d* states at −1.8 eV, corresponding to peak I in the total DOS. The O PDOS displays two main peaks (II and III) observed at −3.4 and −6.1 eV. Two peaks originating from oxygen and one peak from copper have been observed in the XPS spectra at the same energy values. Al PDOS is not shown here because its contribution to valence band is insignificant [49]. There are also Cu 3*d* states between −4.3 and −3.2 eV, indicating a covalent nature in bonding with oxygen. Therefore, valence band mainly consists of states derived from a mixture of Cu 3*d* and O 2*p* orbitals. Antimony has 5*s* and 5*p* orbitals whose energies are very close to O 2*p* and Cu 3*d* states. So the incorporation of antimony in $CuAlO_2$ causes hybridization among Sb 5*s*, 5*p*, and Cu 3*d*, O 2*p* and this hybridization strongly affects the valence band structure. Total DOS and PDOS for SCAO were calculated by ab initio density functional theory, and they are represented in Fig. 8. It has been observed that Sb 5*s* and 5*p* orbitals have significant contribution within the valence band region of CAO. Strong hybridization among the levels leads to a change in their respective energy values. Dominating Cu 3*d* is measured at −4.2 eV instead of −1.8 eV in the case of pure $CuAlO_2$. Whereas O 2p PDOS, observed at −4.1, −6.3, and −9.3 eV, are less than pure $CuAlO_2$.

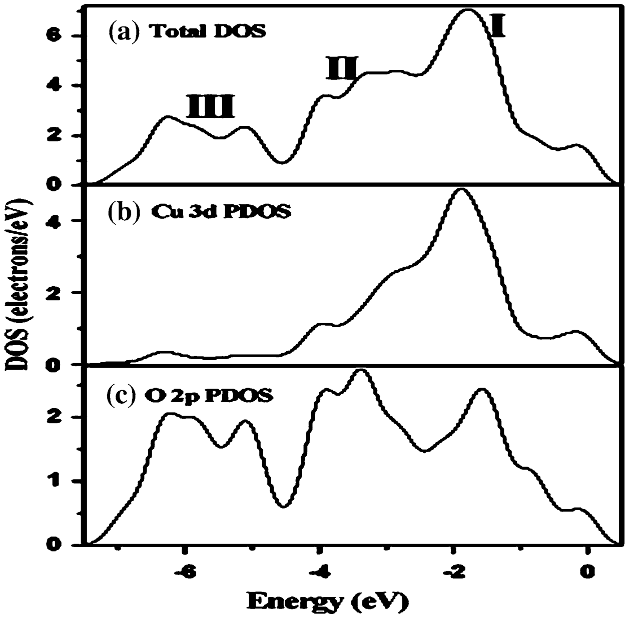

**Fig. 7** **a** Total DOS and **b** and **c** are PDOS of Cu 3*d* and O 2*p*, respectively of CAO

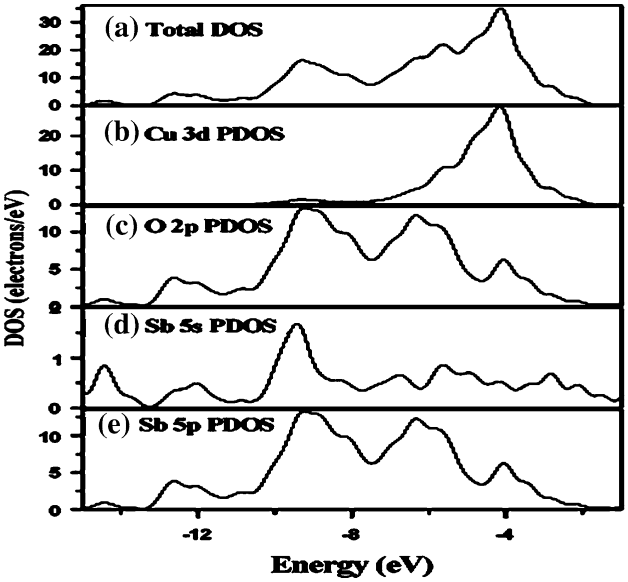

**Fig. 8** **a** Total DOS and **b**, **c**, **d**, and **e** are PDOS of Cu 3*d*, O 2*p*, and Sb 5*s* and Sb 5*p*, respectively of SCAO

## Optical properties

The fundamental absorption, i.e., transition from the valence band to the conduction band can be used to determine the nature and value of the optical band gap. The relation between the absorption coefficient (α) and incident photon energy ($h\nu$) can be written as $(\alpha h\nu)^{1/n} = A\left(h\nu - E_g\right)$, where $A$ is constant, $E_g$ is the band gap of the material under consideration, and the exponent '$n$' depends on the nature of the type of transition. '$n$' = 1/2, 2, and 3/2 for direct allowed, indirect allowed, and direct forbidden transitions, respectively. The plot of $(\alpha h\nu)^{1/n}$ versus $h\nu$ will be straight line for different values of '$n$'; by extrapolating the linear portion of the curve to the $h\nu$-axis, we may obtain the corresponding band gaps. Here, we have calculated the direct band gap of $CuAl_{1-x}Sb_xO_2$ ($x = 0.02$, 0.04, 0.06, 0.08) [50–53] [$(\alpha h\nu)^2$ versus $h\nu$ plot are shown in Fig. 9]. As represented in Table 3, we have found that the band gap of SCAO samples increases from 4.09 to 4.41 eV, with increasing doping concentration from 2 to 8%. From XPS measurement and ab initio calculation based on density functional theory (discussed in previous section), it has been realized that the valence band shifts toward lower energy side due to hybridization between Sb 5*s* and 5*p* and Cu 2*d* and O 2*p* states and consequently the band gap energy increases with Sb doping. We have found the presence of indirect transitions at 4.0, 4.1, 4.23, and 4.33 eV [by plotting $(\alpha h\nu)^{1/2}$ versus $h\nu$ and extrapolating the straight line portions to $(\alpha h\nu)^{1/2} = 0$ on the $h\nu$ axis], respectively. The origin of indirect transitions may be due to the generation of midgap levels due to Sb doping (just above the valence band).

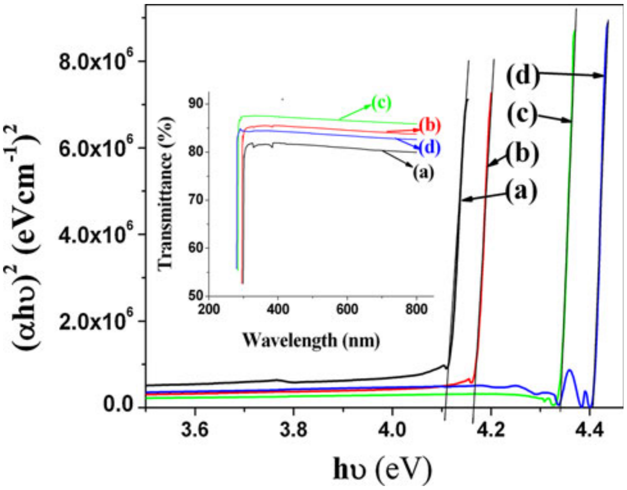

**Fig. 9** Plot of $(\alpha h\nu)^2$ vs. $h\nu$ for (a) 2% (b) 4% (c) 6% and (d) 8% Sb-doped CAO (inset shows the transmittance plot for *a* 2%, *b* 4%, *c* 6%, and *d* 8% Sb-doped CAO samples)

**Table 3** Variation of band gap ($E_g$) with Sb doping

| Doping concentration (in %) | Band gap, $E_g$ (eV) |
|---|---|
| 2 | 4.11 |
| 4 | 4.16 |
| 6 | 4.34 |
| 8 | 4.41 |

## Electrical properties

The electrical characterizations of the Sb-doped $CuAlO_2$ samples were performed by two probe method from room temperature (300 K) to 415 K under vacuum condition ($10^{-5}$ mbar). In Fig. 10, we have plotted ln$\sigma$ versus 1/$T$; the straight line behavior of the plot confirms the semiconducting nature of the samples. Two distinct regions in the *J*–*E* characteristics can be found as shown in Fig. 11. In the low voltage region, the *J*–*E* plots were linear ohmic type, whereas at higher voltage region, nonlinear *J*–*E* plots were observed. The nonlinearity is governed by space charges accumulated at grain boundary regions [54]. To explain the nonlinear behavior of the observed conductivity, we assumed that each CAO grain behaves as a quasi-intrinsic semiconductor, and the conduction process occurs by tunneling of thermally generated holes within the CAO grain through the grain boundaries. In the low field region, current density in the *x*-direction can be expressed by the equation,

$$J_x = ne\mu \int D_x(E)\mathrm{d}E \qquad (4)$$

where $n$ is the concentration of thermally generated free holes in the valence band at thermal equilibrium, and it depends on the effective density of states ($N_v$) of the valence bands. $\mu$ is the intrinsic mobility inside the grain

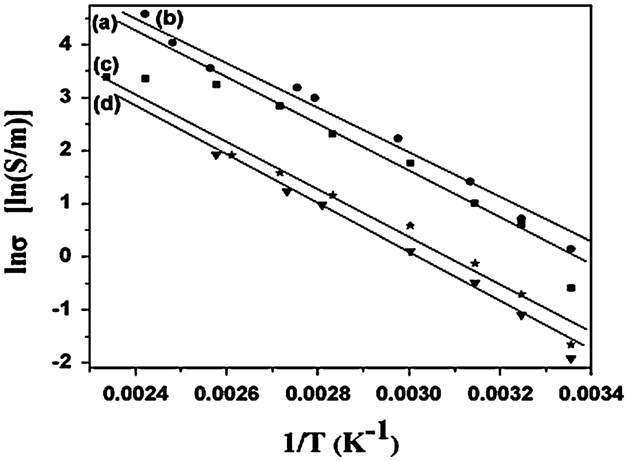

**Fig. 10** ln$\sigma$ versus 1/$T$ for *a* 2%, *b* 4%, *c* 6%, and *d* 8% Sb-doped CAO

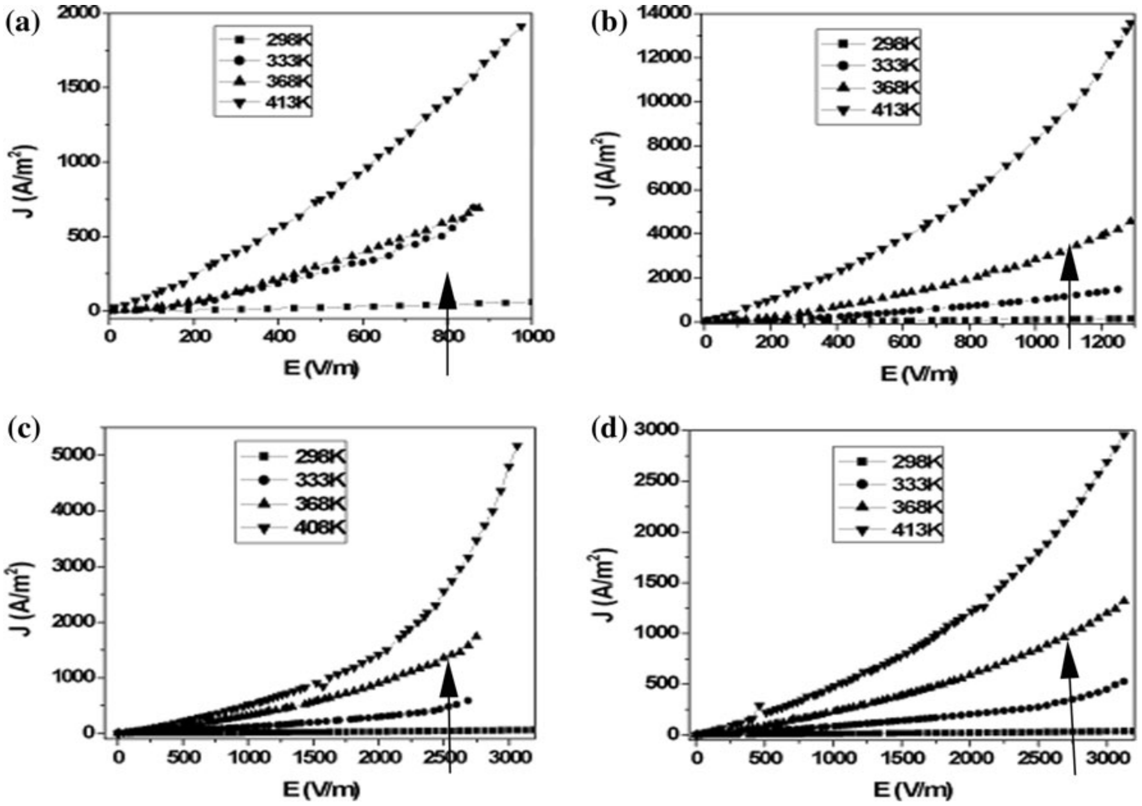

**Fig. 11** *J*–*E* characteristics of **a** 2%, **b** 4%, **c** 6%, and **d** 8% Sb-doped CAO at different temperatures. *Arrows* indicate the voltage for linear–nonlinear transition

and barrier height at the grain boundary [55]. $D_x(E)$ is the transmission probability of the barrier. For small barrier voltage, we can neglect the energy dependence of $D_x(E)$. Within WKB approximation, $D_x(E) = \exp(-2\xi\lambda)$, where $\xi = \left(8\Pi^2 m_1 \varphi h^2\right)^{12}$ and $m_1$ is the effective mass of a charge carrier within the grain boundary region, $\varphi$ represents the barrier height [56, 57]. Therefore, conductivity of a polycrystalline intrinsic semiconductor can be expressed as,

$$\sigma = N_\mathrm{v} e\mu \exp\left(-\frac{E_\mathrm{a}}{kT}\right)\exp(-2\xi\lambda) \qquad (5)$$

where $E_\mathrm{a}$ is the activation energy. From XPS study and ab initio density functional theory-based calculations, we have observed that Sb 5*p* and 5*s* orbitals create levels within the valence band, i.e., Sb doping increases DOS ($N_\mathrm{v}$), hence the electrical conductivity initially increases due to increment in $N_\mathrm{v}$. Similar type of observation was also reported by Seager et al. and Tsurumi et al. [58, 59]. ln$\sigma$ versus 1/*T* curves were fitted with Eq. (5) to obtain activation energy ($E_\mathrm{a}$) within CAO grain. Activation energy increases with doping as shown in Fig. 12. Previous XPS and ab initio DFT calculation revealed that the valence band edge (Cu 3*d* orbitals) shifts toward lower energy side due to the interaction between Sb 5*s* and 5*p* orbitals with the Cu 3*d* orbitals, and this leads to the increment of the activation energy ($E_\mathrm{a}$). Enhancement of $E_\mathrm{a}$ reduces the electrical conductivity in the higher doping region. In the non-ohmic region of conductivity, slopes of ln*I* vs. ln*V* were in the range 1.3–1.6, which clearly shows that the conductivity is mainly space charge limited current (SCLC) controlled by trap levels at grain boundary region. In this field region, current density can be expressed by the equation [60, 61]

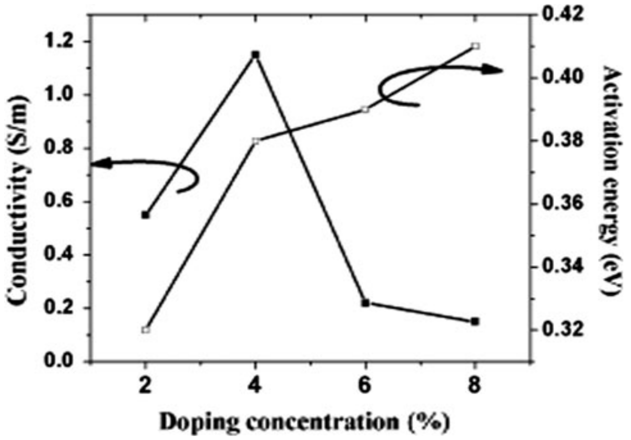

**Fig. 12** Variation of room temperature electrical conductivity and activation energy with doping concentration

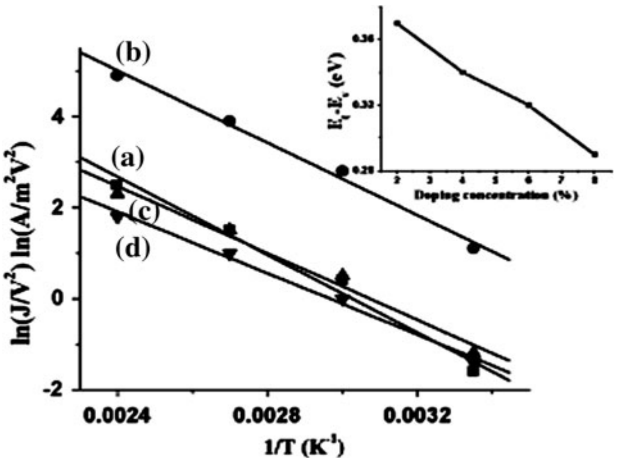

**Fig. 13** Variation of ln($J/V^2$) with temperature *a* 2%, *b* 4%, *c* 6%, and *d* 8% SCAO samples (*inset* shows the variation of $E_t - E_v$ with Sb doping concentration)

$$J_{\mathrm{SCLS}} = \left(\frac{9}{8}\right)\varepsilon\mu\left(\frac{N_v}{N_t}\right)e^{\{-(E_t-E_v)/kT\}}\left(\frac{V^2}{d^3}\right) \quad (6)$$

where $N_t$ represents the density of trapping levels situated at energy $E_t$ above the valence band and ε is the permittivity. Straight line nature of the ln($J/V^2$) versus $1/T$ (for $d = 1$ mm for all the samples) plots as shown in Fig. 13 for $CuAl_{1-x}Sb_xO_2$ ($x = 0.02$, 0.04, 0.06, and 0.08) at the high field non-ohmic region confirms that the current is limited by space charge, accumulated at grain boundary region. Position of trap energy states can be obtained from the slopes of the ln($J/V^2$) versus $1/T$ curves for $CuAl_{1-x}Sb_xO_2$ ($x = 0.02$, 0.04, 0.06, and 0.08). Continuous decrement of the energy difference between the trap states and the top of the valence band ($E_t - E_v$) with respect to doping has been observed (shown in the inset of Fig. 13). As the doping concentration was increased, trap states formed a band, and further increase of doping concentration increases the width of this band that decrease the $E_t - E_v$ with Sb doping.

## Conclusion

In summary, we have successfully synthesized Sb-doped $CuAlO_2$ by solid-reaction technique. Then we have investigated the structural, optical, and electrical properties of Sb-doped $CuAlO_2$. Our results revealed that (i) the crystal structure is not changing with respect to Sb doping (although *a*/*c* ratio changes), (ii) strain is increasing linearly due to larger ionic radius of the dopant atoms compared to the host atom, (iii) band gap increases with Sb doping and this enhancement is well supported from shift of valence band edge measured by x-ray photoelectron spectroscopy and ab initio calculation based on density functional theory, and (iv) in the case of electrical characterizations, a nonlinear variation in conductivity has been observed with respect to Sb doping. The nonlinear *J*–*E* characteristic has also been successfully explained on the basis of space charge accumulation at the grain boundaries. The critical field, at which the nonlinearity starts, increases with doping concentration. The observed nonlinearity in the *J*–*E* characteristics in Sb-doped CAO samples may be useful in the field of power supply network and electrical stress grading at insulator–conductor interface in high voltage application.

**Acknowledgements** One of us (CKG) wishes to thank the Council for Scientific and Industrial Research (CSIR), Government of India, for awarding him a Senior Research Fellowship (SRF) during the execution of the study. One of us (SRP) wishes to thank the University Grants Commission (UGC), Government of India, for awarding him a scholarship during the execution of this study during their M. Tech. course.

## References

1. Laverty SJ, Feng H, Maguire P (1997) J Electrochem Soc 144:2165
2. Yang Y, Wang L, Yan H, Jin S, Marks TJ, Li S (2006) Appl Phys Lett 89:051161
3. Drevillon B, Kumar S, Cabarrocas PR, Siefert JM (1989) Appl Phys Lett 54:2088
4. Emziane M, Durose K, Halliday DP, Bosio A, Romeo N (2005) Appl Phys Lett 87:251913
5. Li YJ, Kwon YW, Jones M, Heo YW, Park Z, Li S (2005) Prog Semicond Sci Technol 20:720
6. Hosono OhtaH, Hayashi K, Hirano M (2003) J Cryst Growth 496:237
7. Tonooka K, Bando H, Aiura Y (2003) Thin Solid Films 445:327
8. Monnier JR, Hanrahan MJ, Apai G (1985) J Catal 92:119
9. Yagi H, Seo W, Koumoto K (2000) Key Eng Mater 251:180
10. Huang H, Tan OK, Lee YC, Tse MS, Guo J, White T (2006) Nanotechnology 17:3668
11. Mattox DM (1991) Thin Solid Films 204:25
12. Dou Y, Fishlock T, Egdell RG, Law DSL, Beamson G (1997) Phys Rev B 55:13381
13. Ramaiah KS, Raja VS, Bhatnagar AK, Tomlinson RD, Pilkington RD, Hill AE, Chang SJ, Su YK, Juang FS (2000) Semicond Sci Technol 15:676
14. Scalvi LVA, Messias FR, Souza AE, Li MS, Santilli CV, Pulcinelli SH (1998) J Sol–Gel Sci Technol 13:793
15. Banerjee AN, Maity R, Kundoo S, Chattopadhyay KK (2004) Phys Status Solid A 201:983
16. Ghosh PK, Maity R, Chattopadhyay KK (2004) Solar Energy Mate Solar Cells 81:279
17. Pelto J, Paajanen M, Kannus K, Lahti K, Harju P (2004, July 5–9) In: International conference on solid dielectrics Toulouse, France
18. Wang X, Xi G, Xiong S, Liu Y, Xi B, Yu W (2007) Cryst Growth Des 7(5):930
19. Kawazoe H, Yasukawa M, Hyodo H, Kurita M, Yanagi HM, Hosono H (1997) Nature 389:939
20. Kykyneshi R, Nielsen BC, Tate J, Li J, Sleight AW (2004) J Appl Phys 96:6188
21. Banerjee AN, Ghosh CK, Chattopadhyay KK (2005) Solar Energy Mater Solar Cells 89:75

22. Banerjee AN, Ghosh CK, Das S, Chattopadhyay KK (2005) Phys B Condens Mater 370:264
23. Banerjee AN, Maity R, Ghosh PK, Chattopadhyay KK (2005) Thin Solid Film 474:261
24. Banerjee AN, Nandy S, Ghosh CK, Chattopadhyay KK (2007) Thin Solid Film 515:324
25. Kizaki H, Sato K, Katayama-Yoshida H (2007) Phys B 462:401
26. Zhang HY, Li PG, Chen CP, Tu QY, Tang WH (2005) J Alloy Comp 396:40
27. Nagarajan R, Uma S, Jayaraj MK, Tate J, Sleight AW (2002) Solid State Sci 4:787
28. Nagarajan R, Duan N, Jayaraj MK, Li J, Vanaja KA, Yokochi A, Draeseke A, Tate J, Sleight AW (2001) Int J Inorg Mater 3:265
29. Banerjee AN, Maity R, Ghosh PK, Chattopadhyay KK (2005) Thin Solid Films 474:261
30. Banerjee AN, Chattopadhyay KK (2004) Appl Surf Sci 225:243
31. Tate J, Ju HL, Moon JC, Zakutayev A, Richard AP, Russell J, McIntyre DH (2009) Phys Rev B 80:165206
32. Koriche N, Bouguelia A, Aider A, Trari M (2005) Int J Hydro Energy 30:693
33. Goe P, Yadav KL (2007) J Mater Sci 42:3928. doi:10.1007/s10853-006-0416-x
34. Kim SH, Lee DH, Park JS, Cho SK, Lee SH, Kim KH (1994) Bull Korean Chem Soc 15:115
35. Tsuji T, Ohashi Y, Yamamura Y (2002) Solid State Ion 541:154
36. Ham FS (1959) J Appl Phys 30:1518
37. Sun CQ, Tay BK, Zeng XT, Li S, Chen TP, Zhou J, Bai HL, Jiang EY (2002) J Phys Condens Mater 14:34
38. Nagle JK (1990) J Am Chem Soc 112:4742
39. Lucovsky G, Whitten JL, Zhang Y (2002) Solid State Electron 46:1687
40. Barton JJ, Coenraad AS, Goddard WA, McGill TC (1980) J Vac Sci Technol 17:1
41. Cullity BD (1979) Elements of x-ray diffraction, 2nd edn. Addison, Wesley
42. Kim KH, Chun JS (1986) Thin Solid Films 141:287
43. Moutinho HR, Al-Jassim MM, Levi DH, Dippo PC, Kazmerski LL (1998) J Vac Sci Technol A 16:1251
44. Chakrabarti R, Ghosh S, Chaudhuri S, Pal AK (1999) J Phys D Appl Phys 32:1258
45. Guha P, Gorai S, Ganguli D, Chaudhuri S (2003) Mater Lett 57:12
46. Moholkar AV, Pawar SM, Rajpure KY, Pati PS, Bhosale CH (2007) J Phys Chem Solids 68:1981
47. Ghosh CK, Popuri SR, Mahesh TU, Chattopadhyay KK (2009) J Sol–Gel Sci Technol 52:79
48. Aston DJ, Payne DJ, Green AJH, Egdell RG, Law DSL, Guo J, Glans PA, Learmonth T, Smith KE (2005) Phys Rev B 72:195115
49. Scanlon DO, Walsh A, Morgan BJ, Watson GW (2009) Phys Rev B 79:035101
50. Ghosh CK, Mitra MK, Chattopadhyay KK (2007) J Appl Phys 101:124911
51. Ghosh CK, Malkhandi S, Chattopadhyay KK (2008) Philos Mag 88:1423
52. Banerjee AN, Ghosh CK, Chattopadhyay KK, Minoura H, Sarkar AK, Akiba A, Kamiya A, Endo T (2006) Thin Solid Films 496:112
53. Banerjee AN, Kundoo S, Chattopadhyay KK (2003) Thin Solid Films 440:5
54. Ruxandra V, Antohe S (1998) J Appl Phys 84:727
55. Muraoka Y, Takubo N, Hiroi Z (2009) J Appl Phys 105:103702
56. Ni J, Arnold E (1981) Appl Phys Lett 39:554
57. Duke CB (1969) Tunneling in Solids, chap. 4. Academic Press Inc, New York
58. Seager CH, Castner TG (1978) J Appl Phys 49:3879
59. Tsurumi T, Nishizawa S, Ohashi N, Ohgaki T (1999) Jpn J Appl Phys 38:3682
60. Bube RH (1960) Photoconductivity of solids. Wiley, New York
61. Gould RD (1982) J Appl Phys 53:3353